

Toward High-Performance Mg-S Batteries via a Copper Phosphide Modified Separator

Yang Yang, Wenbin Fu, Duo Zhang, Wen Ren, Shuxin Zhang, Yuantao Yan, Yang Zhang, Sang-Jun Lee, Jun-Sik Lee, Zi-Feng Ma, Jun Yang, Jiulin Wang, and Yanna NuLi*



Cite This: *ACS Nano* 2023, 17, 1255–1267



Read Online

ACCESS |



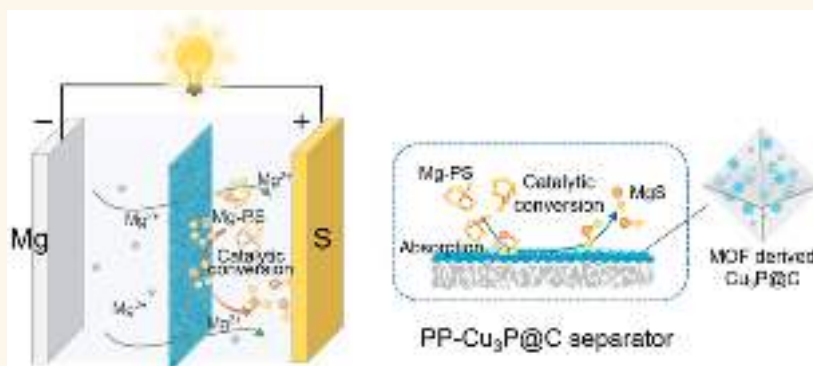
Metrics & More



Article Recommendations



Supporting Information



ABSTRACT: Magnesium–sulfur (Mg–S) batteries are emerging as a promising alternative to lithium-ion batteries, due to their high energy density and low cost. Unfortunately, current Mg–S batteries typically suffer from the shuttle effect that originates from the dissolution of magnesium polysulfide intermediates, leading to several issues such as rapid capacity fading, large overcharge, severe self-discharge, and potential safety concern. To address these issues, here we harness a copper phosphide (Cu_3P) modified separator to realize the adsorption of magnesium polysulfides and catalyzation of the conversion reaction of S and Mg^{2+} toward stable cycling of Mg–S cells. The bifunctional layer with Cu_3P confined in a carbon matrix is coated on a commercial polypropylene membrane to form a porous membrane with high electrolyte wettability and good thermal stability. Density functional theory (DFT) calculations, polysulfide permeability tests, and post-mortem analysis reveal that the catalytic layer can adsorb polysulfides, effectively restraining the shuttle effect and facilitating the reversibility of the Mg–S cells. As a result, the Mg–S cells can achieve a high specific capacity, fast rates (449 mAh g^{-1} at 0.1 C and 249 mAh g^{-1} at 1.0 C), and a long cycle life (up to 500 cycles at 0.5 C) and operate even at elevated temperatures.

KEYWORDS: Mg–S batteries, Cu_3P , functional separator, catalytic, elevated temperature

INTRODUCTION

Rechargeable battery technologies characterized by lithium (Li)-ion batteries have reshaped our daily life, powering the equipment from small electrical devices such as smartphones and laptops to the transportation facilities of electric bikes and vehicles.^{1,2} Meanwhile, as the world dedicates efforts to minimize CO_2 emission, the Li-ion battery production and demand increase year after year. However, there remain several insurmountable challenges, including the energy limits from intercalation materials and chemistry, the limited resources and skyrocketing prices of Li and cobalt (Co) and their compounds, and the pollution from mining these materials.³ To address these challenges, it is crucial to develop alternative battery materials and systems beyond Li chemistry. Among various battery systems, rechargeable magnesium batteries

(RMBs) with metallic Mg as the anode have attracted increasing attention due to the promising characteristics of Mg, including ultrahigh gravimetric and volumetric capacity (2205 mAh g^{-1} and 3833 mAh cm^{-3} , theoretically),⁴ low redox potential (-2.37 V versus SHE),⁵ high crustal abundance ($\sim 2.3 \text{ wt } \%$, 1300+ times higher than that of Li),^{6–8} low price (100 times lower than Li price by weight), high operation

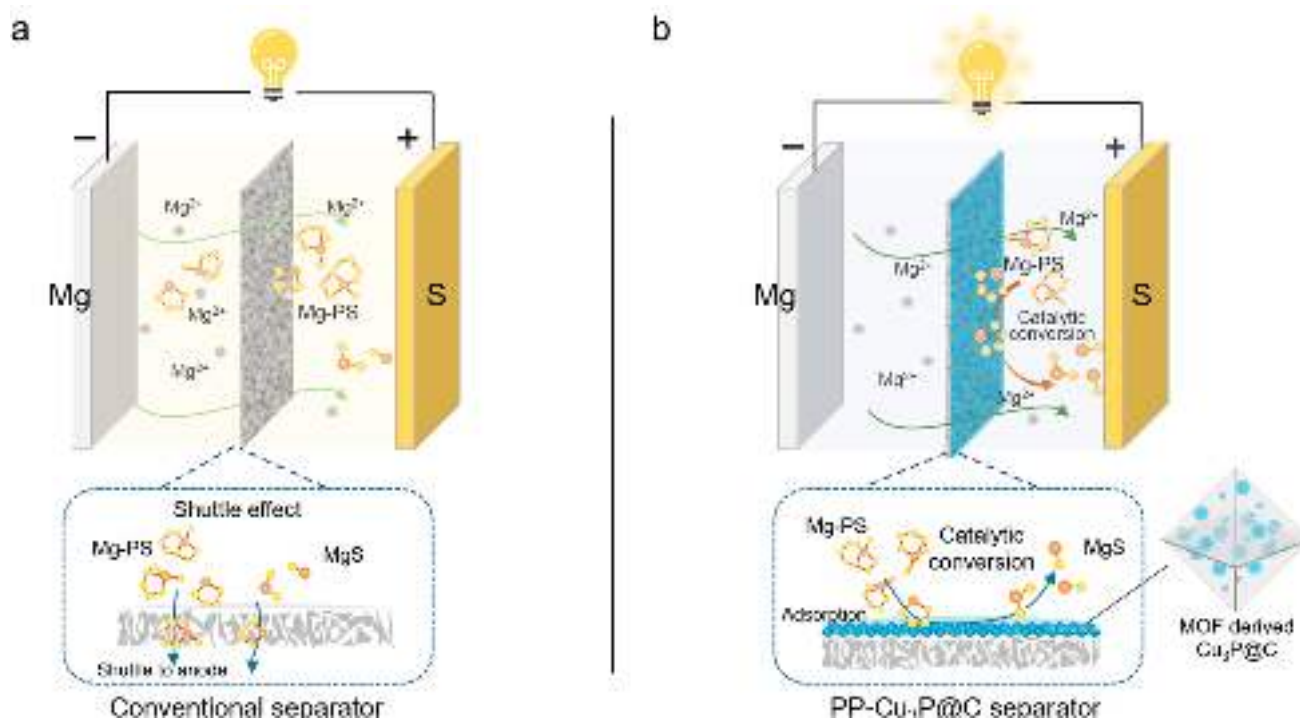
Received: September 18, 2022

Accepted: December 27, 2022

Published: December 30, 2022



Scheme 1. Schematics of Mg-S Cells and Function of Separators: (a) Conventional Separators for Mg-S Batteries Resulting in a Shuttle Effect Due to the Dissolution of Mg Polysulfides (Mg-PS); (b) a Functionalized Separator with $\text{Cu}_3\text{P@C}$ to Address These Issues through Its Catalytic Conversion and Adsorption



safety, and environmental benignity.^{9–11} Over the past decade, studies of RMB cathodes have focused on intercalation materials (such as Chevrel phase, layered oxides, phosphates, etc.)^{12,13} and conversion materials featuring sulfur (S) and selenium (Se),^{14–16} which can provide much higher capacity compared to intercalation cathodes. S (also denoted S_8) has been widely investigated in Li and Na battery systems, considering its ultrahigh theoretical capacity (1673 mAh g^{-1}) and very low cost ($\sim \$0.09/\text{kg}$ in 2021).^{17,18} Recent studies have already explored S or S-based composites for RMB cathodes and achieved aspirational specific capacity.^{19–21} Therefore, it is highly desirable to advance Mg-S batteries to realize a low-cost but high-performance battery system.

Similar to the Li-S system, Mg-S batteries also employ the multiple-step transition of S_8 to long-chain magnesium polysulfide (Mg-PS) intermediates, including MgS_8 , MgS_6 , and MgS_4 , followed by short-chain sulfides such as MgS_2 and MgS as the final products after being fully discharged.^{20,22} Long-chain Mg-PS could be soluble in electrolyte solvents and penetrate through porous separator to the anode, like the “shuttle effect” in Li-S or Na-S batteries,^{23,24} resulting in capacity degradation, self-discharge, thermal runaway, and safety concerns.²⁵ To address this notorious issue regarding the shuttle effect, over the past few years, great efforts have been focused on the confinement of sulfur into a stable host (such as porous carbon, conductive polymers),^{26–28} the introduction of stable electrolytes or additives (such as new Mg salts, Li salt additives, stable solvents),^{21,29} and the development of stable Mg anodes (such as a Mg-based alloy with a liquid metal Ga layer).^{30,31} Despite these advances, however, the achieved performance of Mg-S batteries needs to be further improved, considering that most of them show serious capacity decay after only being cycled for less than 100 times.

Separators between cathodes and anodes play a vital role in ionic conduction and electronic insulation in batteries. Traditional Li-ion battery separators made from polyolefins such as polypropylene (PP) and polyethylene (PE)³² could suffer from low thermal stability and poor wettability, as well as the HF attack from the decomposition of LiPF_6 electrolytes with cycles.^{33,34} Recently, advanced separators coated with ceramic materials have been well developed and commercialized in the battery market to address these issues.^{34,35} Over the past decade, attempts to build a stable interlayer or functional separator have shown great promise for mitigating the shuttle effect in alkali-metal-sulfur batteries.^{36–38} This could indeed provide us with a possible solution to minimize the Mg-PS shuttle and improve the reversibility of Mg-S batteries through engineering the separator surface. Recently, a Mg-S battery containing a modified separator with polyoxometalate delivered a high specific capacity of 320 mAh g^{-1} after 100 cycles because of the polysulfide shuttle inhibition and the reactivation of the polysulfide species.³⁹ Using Mo_6S_8 as a functional layer achieved a superior adsorption capability of polysulfides, which enabled Mg-S cells to be cycled at 0.2 C for 200 cycles with a Coulombic efficiency of 96%.⁴⁰ Unfortunately, all of these cells still cannot avoid a rapid capacity degradation upon cycling and their lifespans are consequently limited to 100–200 cycles.

Metal phosphides present excellent performance for use in battery electrodes and electrocatalysts due to their high electrical conductivity and electroactivity,^{41–43} which could provide advantageous metrics for being a separator stabilizer for Mg-S batteries. For a proof-of-concept study, here we report on a functional separator based on adsorptive and catalytic copper phosphide (Cu_3P) that can overcome the issues in Mg-S batteries through minimizing polysulfide dissolution and facilitating the reversibility of the conversion

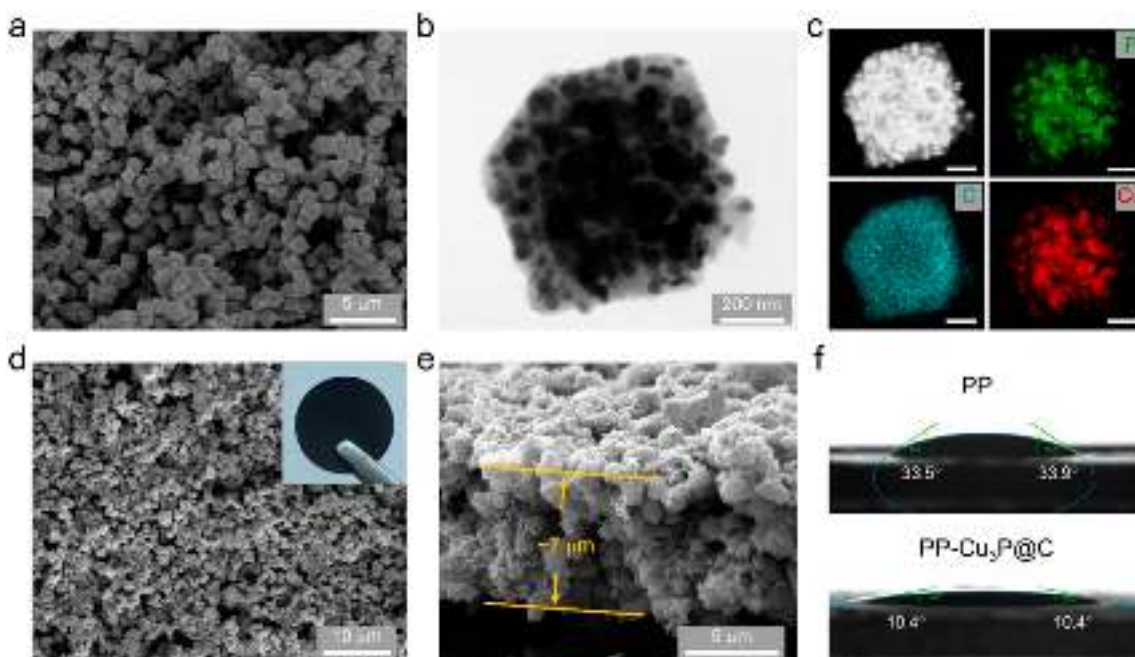


Figure 1. Physical characterizations of $\text{Cu}_3\text{P}@C$ and its coated separator. (a) SEM of $\text{Cu}_3\text{P}@C$ nanocomposites. (b) TEM image of a single $\text{Cu}_3\text{P}@C$ octahedron. (c) EDS mappings of P, C, and Cu for the micro-octahedron. Scale bars: 200 nm. (d, e) Surface and cross-section SEM images of PP- $\text{Cu}_3\text{P}@C$ separator. The inset of d) is a visual photo of the separator. (f) Contact angle tests for PP and PP- $\text{Cu}_3\text{P}@C$ separators with a drop of the electrolyte solution.

reaction. This functional catalytic layer is constituted of nanoconfined Cu_3P in a carbon matrix ($\text{Cu}_3\text{P}@C$), which is derived from a metal–organic framework (MOF). The $\text{Cu}_3\text{P}@C$ composite is built on a porous PP membrane to form a porous bifunctional membrane with high electrolyte wettability and good thermal stability. Density functional theory (DFT) calculations and polysulfide permeability tests reveal that the catalytic layer can effectively adsorb polysulfides and largely reduce the shuttle effect. As a result, the Mg-S cells based on the PP- $\text{Cu}_3\text{P}@C$ separator achieve a higher specific capacity, faster rates, and better cycle stability (up to 500 cycles) than the cells with bare PP. Especially, the Mg-S cells based on the bifunctional separator also show excellent electrochemical properties even at elevated temperatures. Furthermore, Mg-S pouch cells based on the functional separator were demonstrated for potential applications.

RESULTS AND DISCUSSION

Fabrication of Functionalized Separator. In general, Mg-S cells consist of a Mg anode, a S (or S-based composite) cathode, and a porous polymer separator membrane filled with liquid Mg-salt electrolyte, as illustrated in Scheme 1. Conventional Mg-S cells suffer from the shuttle effect resulting from the dissolution of magnesium polysulfide (Mg-PS) intermediates, which could lead to several issues including a rapid capacity degradation, increasing interfacial resistance, and severe self-discharge of the cells (Scheme 1a). We expect that these issues can be addressed via using a bifunctional separator with an adsorptive and catalytic coating layer (Scheme 1b). The coating layer is constructed from a stable phosphide nanocomposite with Cu_3P confined in a carbon matrix ($\text{Cu}_3\text{P}@C$), in which air-stable Cu_3P nanoparticles are electrically conductive and active, and they can adsorb S-based species and catalytically convert soluble Mg-PS to insoluble compounds such as MgS_2 and MgS (Scheme 1b).

Besides, the carbon matrix can serve as an adsorption mediator to sulfur species as well as a physical barrier to prevent polysulfides from penetrating or blocking the porous separator. In addition, the functional separator with the Cu_3P -based layer can also possess other promising features, including higher wettability and better thermal stability than the conventional PP separator. As such, Mg-S cells would achieve a high capacity and a long cycle life even at elevated temperatures, which is desirable for many potential applications.

As a coating material for the separator, the $\text{Cu}_3\text{P}@C$ nanocomposite was derived from carbonization and phosphidation of a copper metal–organic framework (MOF), copper benzene-1,3,5-tricarboxylate (Cu-BTC) micro-octahedra. Cu-BTC was synthesized through a coprecipitation method,⁴⁴ considering that it can fabricate a highly crystallized and microporous structure for many MOFs.^{45,46} After carbonization, Cu-BTC was decomposed to form a composite consisting of metallic Cu nanoparticles impregnated in a carbon matrix. The phase feature of Cu (JCDPS #04-0836) can be confirmed by X-ray diffraction (Figure S1a in the Supporting Information). Since nano Cu is very active, it can easily react with the phosphine gas (released during the decomposition of NaHPO_2 at high temperatures). The phosphidation successfully converted Cu into Cu_3P (JCPDS #71-2261), as revealed by XRD (Figure S1b).

Scanning electron microscopy (SEM) depicts that the produced $\text{Cu}_3\text{P}@C$ composite shows a uniform morphology of micro-octahedra (Figure 1a), similar to their precursors before phosphidation (Figure S2). These micro-octahedra exhibit sizes of 1–2 μm and contain many nanocrystallized Cu_3P particles confined by a carbon frame, as observed from transmission electron microscopy (TEM, Figure 1b). The scanning TEM (STEM) together with EDS mappings for a random octahedron (Figure 1c) clearly presents the locations of Cu_3P crystals as white dots/shapes, matching well with the

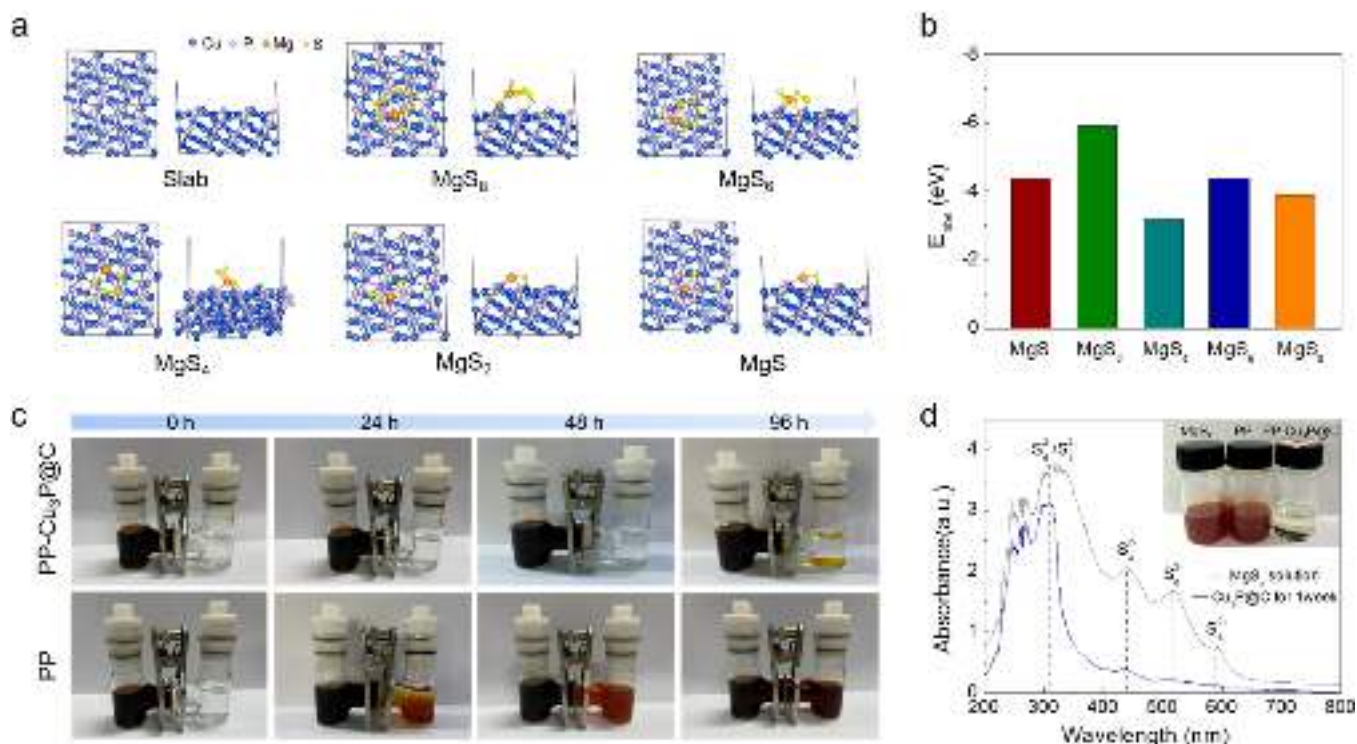


Figure 2. Computation and permeability tests of polysulfides. (a) Optimized geometries of MgS_x ($x = 8, 6, 4, 2, 1$) species adsorption at the Cu_3P phase surface. (b) Adsorption energies of MgS_x to Cu_3P crystal structure. (c) Polysulfide permeation tests for PP- $\text{Cu}_3\text{P}@C$ and PP separators. (d) UV-vis spectra and visual photo (inset) of the MgS_x solutions before and after exposure to PP- $\text{Cu}_3\text{P}@C$ and PP separators for 1 week.

overlap from the element mappings of Cu and P, in contrast to C distribution covering all of the profile. This further indicates that the Cu_3P nanoparticles are well sealed in the carbon matrix. Based on thermogravimetric analysis (TGA), we find that the mass fraction of Cu_3P is ~ 42 wt % in the $\text{Cu}_3\text{P}@C$ composite (Figure S3). From N_2 adsorption-desorption tests, the obtained isotherms show type IV curves with a H2 hysteresis loop (Figure S4a), indicating the presence of slit-shaped mesopores. The Brunauer-Emmett-Teller (BET) surface area is calculated to be $\sim 120 \text{ m}^2 \text{ g}^{-1}$, and the average pore size is $\sim 3.5 \text{ nm}$ (Figure S4b), according to the Barrett-Joyner-Halenda (BJH) model. These structures could offer effective sites for adsorption/binding of sulfur species on the modified separator, which thus works as a physical barrier to reduce the shuttle of polysulfides through the separator to the anode.

To produce a functionalized separator, we mixed the $\text{Cu}_3\text{P}@C$ nanocomposite with a small amount of carbon black (5 wt %) and PVDF-HFP (5 wt %) to form a homogeneous slurry. Then the slurry was coated onto the PP membrane surface (details in the Experimental Section) to form a bifunctional separator membrane with an asymmetric structure. The inset of Figure 1d shows that the top surface of the PP- $\text{Cu}_3\text{P}@C$ membrane is covered by a dark layer without any cracks, in contrast to the white uncoated PP membrane with obvious pores (Figure S5). The functional coated membrane is still strong enough and has a good mechanical stability to survive structural deformation upon folding or scratching, which is expected for a separator used in practical applications. SEM shows that the coating layer consists of well-distributed $\text{Cu}_3\text{P}@C$ micro-octahedra and much smaller particles of carbon black (Figure 1d), and they are homogeneous and interconnected via

the PVDF-HFP binder to form a porous layer. The cross-section SEM image indicates that the $\text{Cu}_3\text{P}@C$ coating layer has a thickness of $\sim 7 \mu\text{m}$ (Figure 1e). A coating layer less than $7 \mu\text{m}$ is too thin to control the quality for a full coverage, while an increase in the coating thickness could reduce the porosity and hinder battery rate capability and cycle performance. Considering small voids among the different-sized particles, the resulting coating layer is porous, and it could not only work as a barrier to block the permeation of polysulfides through the separator but also ensure the electrolyte wetting and ion diffusion. The other side of the membrane facing the anode is PP, which can provide a strong support and prevent a short circuit between the two electrodes. In addition, the coating layer is found to improve the electrolyte wettability of the separator due to a small surface contact angle with the electrolyte. After coating, the surface contact angle of the membrane can be reduced from 33.5° to 10.4° , along with a larger wetting area compared to a bare PP membrane (Figure 1f). The excellent wettability is expected to have more electrolyte uptake and enhance ion transport.

Computation and Permeability Tests of Polysulfides.

To reveal the interactions between Cu_3P and Mg polysulfides and theoretically understand how the separator functions on the adsorption and conversion of polysulfides, we employed the Vienna ab initio simulation package (VASP) to perform density functional theory (DFT) calculations within the generalized gradient approximation (GGA) using the Perdew-Burke-Ernzerhof (PBE) formulation.^{47–49} We created a supercell of Cu_3P for its surface adsorption/binding of different MgS_x ($x = 1, 2, 4, 6, 8$), as illustrated in Figure 2a. After optimization, the surface adsorption energy (E_{ads}) was calculated based on the equation:

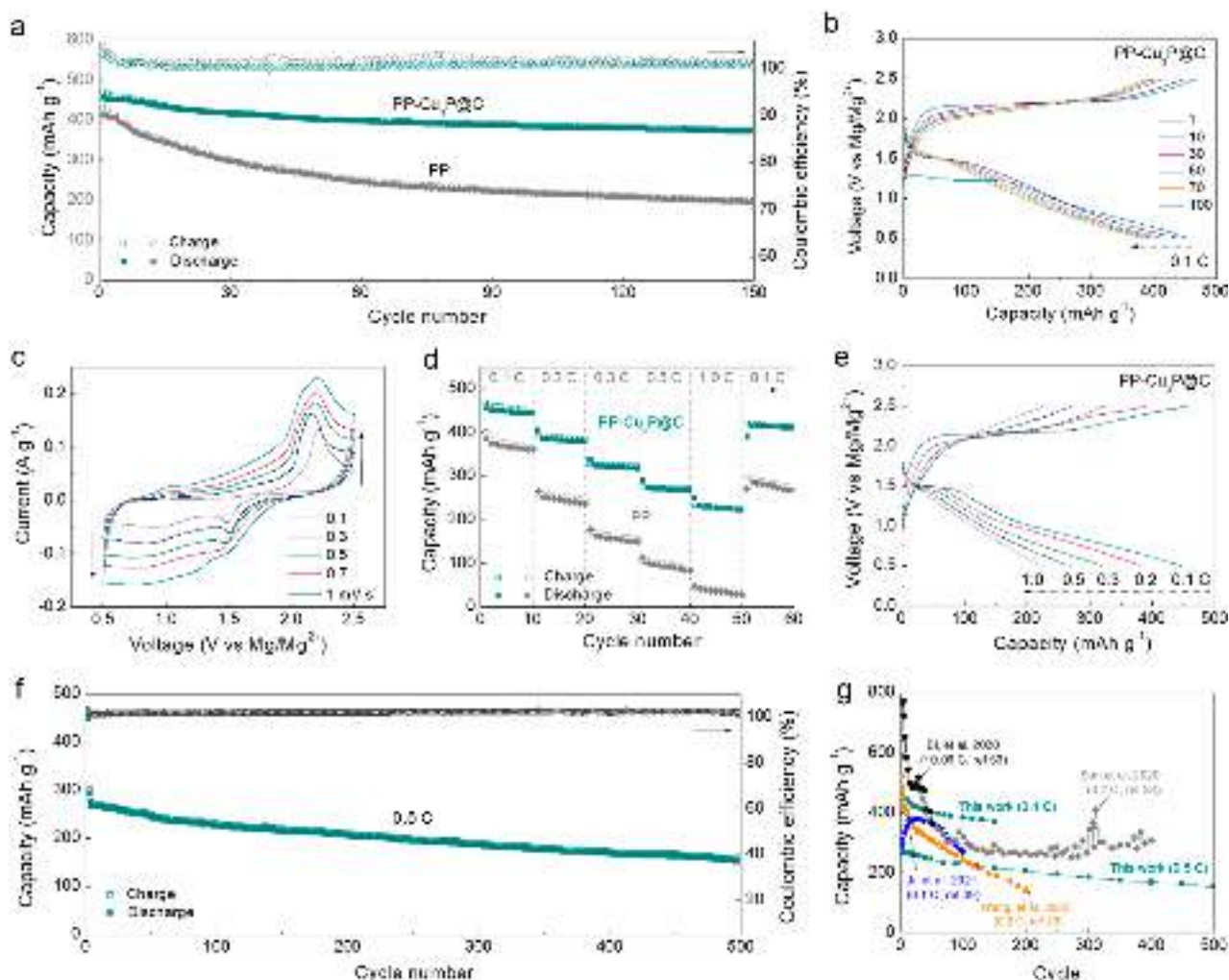


Figure 3. Electrochemical performance of Mg-S cells. (a) Cycle stability of Mg-S cells with PP and PP-Cu₃P@C separators at a current rate of 0.1 C. (b) Charge–discharge profiles of the PP-Cu₃P@C based cell at different cycles. (c) CV scans of the Mg-S cell with PP-Cu₃P@C separator from 0.1 to 1 mV s^{−1}. (d) Rate comparison of cells with different separators. (e) Charge/discharge profiles of the PP-Cu₃P@C cell at different rates. (f) Long-term cycle stability of the PP-Cu₃P@C-based cell at 0.5 C. (g) Cycle life in this work compared with those in prior studies.

$$E_{\text{ads}} = E_{\text{tot}} - E_{\text{surf}} - E_{\text{MgS}_x} \quad (1)$$

where E_{tot} is the slab energy for a given surface (single point or relaxed surface) and E_{surf} is the energy of the relaxed surface geometry per formula unit. According to the calculations, all the energy values for Cu₃P interacted with polysulfides are summarized in Table S1 (Supporting Information). The adsorption energies (E_{ads}) for polysulfides MgS, MgS₂, MgS₄, MgS₆, and MgS₈ are −4.384, −5.911, −3.183, −4.383 and −3.899 eV, respectively (Figure 2b). It is noted that MgS₂ among them shows the smallest (or the most negative) value, which means that MgS₂ is likely to have a stronger adsorption on Cu₃P. Besides MgS₂, the E_{ads} values for MgS₆ and MgS₈ are also relatively small, indicating a possible adsorption binding between Cu₃P and these intermediates. For comparison, we additionally built a polysulfide-interaction model with the monovalent copper compound Cu₂S, as shown in Figure S6a. Taking MgS₄ for example, the E_{ads} value of Cu₂S-MgS₄ is −2.501 eV, larger than that of Cu₃P-MgS₄ (−3.183 eV), implying that the binding effect of Cu₃P for polysulfides could be stronger than that of Cu₂S. From their density of state (DOS) plots (Figure S6b), the contribution from the p orbitals

of the P and S atoms should also be taken into account, except for the d band of the Cu atom. The energy center of the p band in Cu₃P significantly shifts to the Fermi level, and the energy gap of Cu₃P between the energy centers of the Cu 3d and P 2p bands is calculated to be 1.42 eV, smaller than that of Cu₂S (1.88 eV), in agreement with previous reports.^{50–52} The smaller band gap enables Cu₃P to have a more effective function on polysulfides, promoting the electron transfer and facilitating the polysulfide transformation, as was the case for the metal phosphide previously reported in Li-S systems.^{53,54} Therefore, it is expected that Cu₃P has a better adsorption and catalytic performance of polysulfides than other Cu compounds in Mg-S cells.

We conducted permeability tests of Mg polysulfides through different separators. As shown in Figure 2c, a U-shaped glass bottle with two sides separated by a separator membrane (PP-Cu₃P@C or PP) inside the bridge channel was filled with 0.1 M MgS_x/1,2-dimethoxyethane (DME, the solvent of the electrolyte) solution on the left side and pure DME on the right side. MgS_x was prepared using a ball-milling method.⁵⁵ From the beginning (0 h) to 24 h, it should be noted that the right side of the U-shaped glass bottle with the PP-Cu₃P@C

separator was clean, while that with a bare PP separator underwent a color change due to the MgS_x diffusion from the MgS_x/DME solution to pure DME. After standing for 96 h, the right side of the bottle using a PP- $\text{Cu}_3\text{P}@C$ separator still remained clean, with only trace amounts of MgS_x passed through the membrane, in contrast to the deep brown solution for the PP-based setup. This indicates that the coating layer based on Cu_3P is able to serve as an efficient barrier to the permeation of polysulfides through the membrane. To further reveal the differences of their chemistry in addition to the color change, we conducted ultraviolet–visible (UV–vis) spectroscopy to scan the solutions after exposure to different separators. An inset in Figure 2d displays MgS_x/DME solutions before and after exposure to PP- $\text{Cu}_3\text{P}@C$ and PP separators for 1 week. The obtained UV–vis adsorption spectra show much weaker peaks of S_4^{2-} , S_6^{2-} , and S_8^{2-} for the solution after exposure to the PP- $\text{Cu}_3\text{P}@C$ separator, which indicates that the separator has a strong adsorption ability toward polysulfides. All of these results can suggest that the functional separator has a great potential to minimize the shuttle of Mg polysulfides and improve Mg–S cell performance.

Electrochemistry of Functionalized Separator. To explore the electrochemical performance of Mg–S cells with the Cu_3P -functionalized separator, we assembled coin cells by using the sulfur/carbon composite as the cathode, Mg foil as the anode, and a fluorinated alkoxyborate Mg salt, $\text{Mg}[\text{B}(\text{Ohfp})_4]_2$ (magnesium tetrakis(hexafluoroisopropoxy)borate), dissolved in DME as the electrolyte. The electrolyte was prepared based on a coordination chemistry reaction,⁵⁶ as detailed in the Experimental Section. This magnesium electrolyte enables a weak coordination of the $\text{Mg}[\text{B}(\text{Ohfp})_4]_2$ salt with DME molecules, demonstrating a good (electro)-chemical stability and high ionic conductivity.⁵⁷ The sulfur/carbon composite for cathode was produced based on a melt-diffusion method that allowed S to be confined in ordered mesoporous carbon (CMK-3) to uniformly form a nanocomposite of S/CMK-3 (detailed in the Experimental Section). Its morphology and chemical distribution were further confirmed by SEM and EDS (Figure S7). In the produced composite (S/CMK-3), the mass fraction of S is calculated to be $\sim 54\%$, as confirmed by its TGA (Figure S8). The produced S/CMK-3 was mixed with Super-P and PVDF to form a slurry and was then coated on a carbon-coated aluminum foil as the cathode. The specific capacities of Mg–S cells were calculated based on the mass of S.

The assembled cells were first cycled with a voltage window of 0.5–2.5 V (vs Mg/Mg^{2+}) at a current rate of 0.1 C (1 C = 1673 mA g^{-1}). Figure 3a compares the cycling performance of Mg–S cells based on PP- $\text{Cu}_3\text{P}@C$ and PP. It is obvious that the PP- $\text{Cu}_3\text{P}@C$ cell can show a much better cycle stability and lower overcharge and Coulombic efficiency (CE; charge capacity is divided by discharge capacity), together with a higher specific capacity than the PP-based cell at each cycle. The PP- $\text{Cu}_3\text{P}@C$ cell exhibits an initial discharge capacity of 456 mAh g^{-1} , corresponding to a CE of 103.1%, and its capacity can still keep up to 371 mAh g^{-1} (a retention of $\sim 81.3\%$) with a CE of 100.8% after 150 cycles. As a sharp contrast, the discharge capacity of the PP-based cell degrades from 411 mAh g^{-1} with 105.0% CE at the first cycle to 196 mAh g^{-1} with 101.3% CE at the 150th cycle. A higher capacity retention and lower overcharge for the PP- $\text{Cu}_3\text{P}@C$ cell implies that the functional coating layer can effectively suppress the shuttling of Mg-PS, in agreement with the

polysulfide permeation tests in Figure 2c. To understand the electrochemical redox reaction in Mg–S cells, we compared their voltage profiles at different cycles (Figure 3b and Figure S9a). It is worth noting that the discharge/charge curves can correspond to the magnesiation/demagnesiation of sulfur including the typical multistep reduction reaction from the starting sulfur (S_8) to the soluble intermediates and to the final products MgS_2/MgS , and then vice versa. The discharging voltage plateau located around 1.50 V and charging voltage plateau at 2.16 V could be related to the transition from S_8 and $\text{MgS}_8\text{--MgS}_4$, and MgS_2/MgS to S_8 , respectively. The voltage plateau for the PP separator shows a lower discharging position at 1.30 V and higher charging plateau at 2.23 V (Figure S9a), along with a higher voltage hysteresis, which could be attributed to a larger interfacial resistance. The smaller voltage polarization between charging and discharging plateaus for PP- $\text{Cu}_3\text{P}@C$ suggest that the functional layer as a conductive barrier layer can improve the sulfur utilization by reducing the internal resistance of the coin cell. The redox peaks in CV scans can match well with their charge/discharge profiles (Figure S10). The anodic peaks gradually shift toward 1.50 V, with the cathodic peaks shifting toward 2.10 V. From different CV scans, much higher current densities and lower peak potential differences of the PP- $\text{Cu}_3\text{P}@C$ cell further demonstrate a faster redox conversion and more reversible electrochemical process than the PP cell, resulting from both the high surface coverage of Mg polysulfides and low charge transfer resistance at the interface. As the scan rate increases (Figure 3c), the CV of the cell with the PP- $\text{Cu}_3\text{P}@C$ separator shows incremental integrated area and broad peaks, indicating fast charge storage and good rate capability. The larger voltage polarization represented in the first cycle may result from the sluggish conversion of some insulating sulfur, which is activated with a decreased polarization after subsequent scanning. Besides, we find that the capacity contribution from the $\text{Cu}_3\text{P}@C$ coating layer can be ignored in Mg–S cells, considering the much larger CV profile area of S/CMK-3 compared to that of $\text{Cu}_3\text{P}@C$ as a cathode (Figure S11).

We further evaluated their rate capability by charging/discharging these cells from 0.1 to 1.0 C (Figure 3d). As expected, the cell based on PP- $\text{Cu}_3\text{P}@C$, compared to PP, exhibited better performance at each rate. The stable discharge capacities are 449, 405, 336, 291, and 249 mAh g^{-1} , respectively, as the applied rate varies from 0.1, to 0.2, 0.3, 0.5, and 1.0 C. When the current rate was switched to 0.1 C after 50 cycles, its capacity could also recover to 420 mAh g^{-1} , which is much better than that of the PP-based cell ($\sim 280 \text{ mAh g}^{-1}$ at 0.1 C reset after 50 cycles). From the charge/discharge profiles at different rates (Figure 3e), they still present magnesiation/demagnesiation plateaus similar to those at a low rate in Figure 3b, indicating the highly reversible electrochemical reaction between the Mg anode and S/CMK-3 cathode. As a sharp contrast, the charge/discharge profiles of the PP cell undergo a rapid capacity decay and voltage drop as the rate increases (Figure S9b). To evaluate their long-term performance, we further cycled the cell at a high rate of 0.5 C, with a stabilization step using 0.1 C for first 2 cycles. As shown in Figure 3f, the Mg–S cell based on PP- $\text{Cu}_3\text{P}@C$ can stably operate and maintain a high specific capacity of 152 mAh g^{-1} after 500 cycles, with a very small decay of 0.097% (0.28 mAh g^{-1}) per cycle. It is desirable that our results are better than those of previous studies on Mg–S cells (Figure 3g), including prior works on modified separators with polyoxometalate³⁹

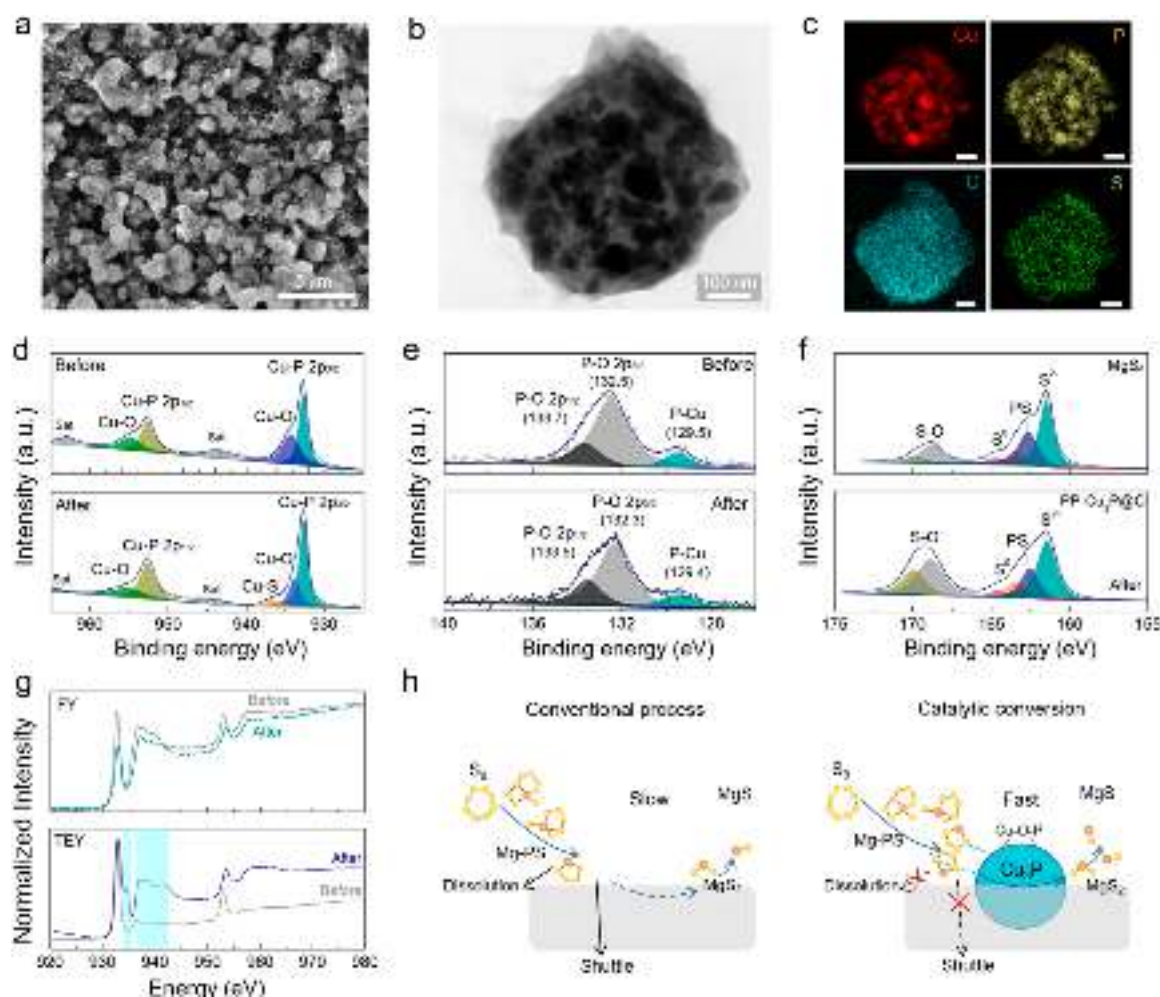


Figure 4. Post-mortem characterizations. (a) SEM image of the PP-Cu₃P@C separator after 150 cycles. (b) TEM image of a single particle of a Cu₃P@C octahedron scratched from the cycled separator. (c) EDS mappings of P, Cu, C, and S for a cycled Cu₃P@C single particle. Scale bars: 100 nm. XPS spectra of (d) Cu 2p and (e) P 2p of the PP-Cu₃P@C separator before and after cycling. (f) XPS spectra of S 2p for the cycled separator and as-prepared MgS_x. (g) Soft XAS of the Cu element from FY and TEY scan modes for the PP-Cu₃P@C separator before and after cycling. (h) Schematics of the transformation from sulfur (S₈), polysulfides to MgS₂/MgS at the cathode–separator interface: conventional process (left) versus catalytic conversion (right).

and Mo₆S₈,⁴⁰ as well as other improvement methods such as introducing an active host for the sulfur cathode⁵⁸ and an ionic liquid electrolyte.⁵⁹ These results shed light on our functional PP-Cu₃P@C separator with great application potentials toward next-generation Mg-S cells.

Electrochemical impedance spectroscopy (EIS) allows us to get insight into the charge/ion transport kinetics at the electrodes, separator, and their interfaces. The Cu₃P@C layer on the PP separator maintains a good ionic conductivity due to moderate internal resistance and good porosity. This can be well confirmed by the ionic conductivity tests from the stainless-steel (SS) symmetric cells with the pristine and modified separators using EIS. Based on the tests, the ionic conductivity (σ) of PP-Cu₃P@C in Mg[B(OHfp)₄]₂/DME electrolyte is 0.27 mS cm⁻¹, slightly higher than that for the PP separator (0.24 mS cm⁻¹) (Figure S12). Furthermore, the obtained Nyquist plots of the Mg-S cells before and after cycling can be fitted with an equivalent circuit, as shown in Figure S13. The x intercept in the high-frequency region is related to the series resistance (R_s) including the intrinsic electronic properties of the electrodes and the contact resistance for cell components such as electrodes, separator,

electrolyte, etc. The semicircle in the middle-frequency region corresponds to the charge-transfer resistance (R_{ct}), and the inclined line in the low-frequency region is associated with the diffusion kinetics of Mg²⁺ ions in the S/CMK-3 cathode. Both separators show small R_s values, indicating good physical contacts for cell components. R_{ct} in the PP-based cell increases obviously from 167.7 to 325.0 Ω before and after cycling, while the PP-Cu₃P@C cell shows a very small change (from 98.2 to 114.4 Ω) during cycling. This demonstrates that the bifunctional Cu₃P@C layer can effectively prevent the dissolution of polysulfides and provide fast pathways for charge transfer, guaranteeing the good reversibility of the Mg-S cell upon cycling.

Post-Mortem Analysis. To further reveal that the shuttling of polysulfides is suppressed by the functional separator, we disassembled the cells after cycling (for 150 cycles) and conducted a post-mortem analysis regarding their morphology and chemistry. It was found that the surface of the separator facing toward the S cathode (the Cu₃P@C face) can preserve its initial microstructures (Figure 4a–c). The surface becomes mossy (Figure 4a) because of the polymer binder coated on the surface. A TEM image (Figure 4b) reveals that

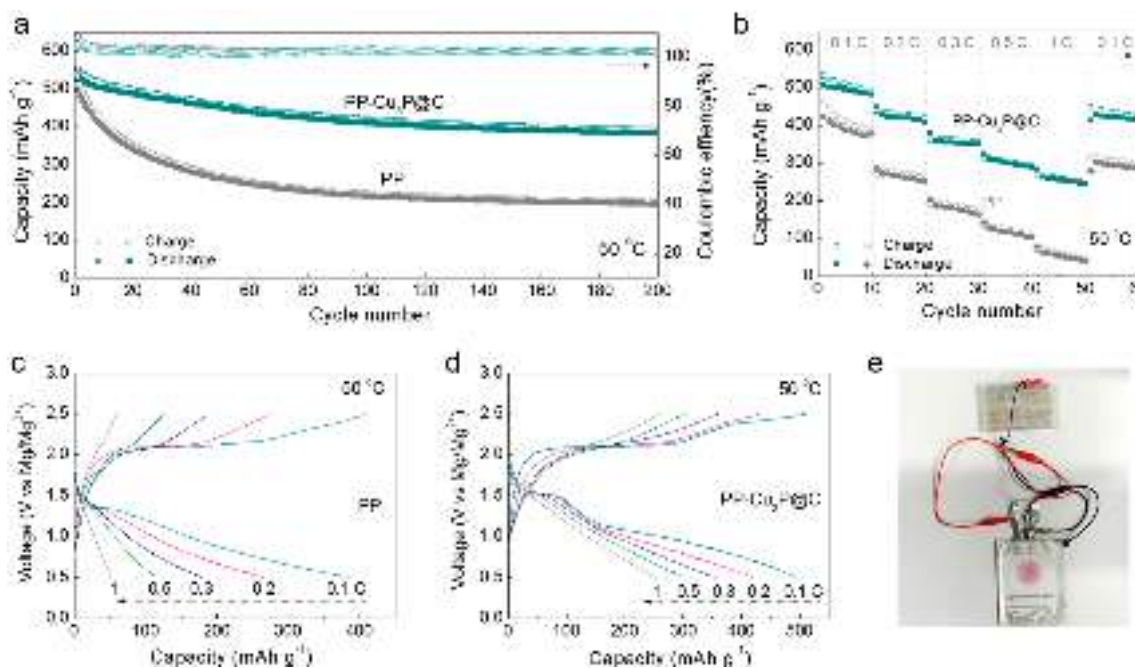


Figure 5. Electrochemical performance of Mg-S cells at an elevated temperature of 50 °C. (a) Cycle stability of Mg-S cells with different separators at 50 °C. (b) Rate comparison of cells with different separators at 50 °C. Charge/discharge voltage profiles of (c) a PP-based cell and (d) PP-Cu₃P@C-based cell at different rates and 50 °C. (e) Photo of a PP-Cu₃P@C-based Mg-S pouch cell.

the particle profile of Cu₃P remains unchanged, similar to its fresh status in Figure 1b. The EDS mappings of S and C elements show good overlap of profiles (Figure 4c), which could be attributed to the sulfur species adsorption from its carbon matrix structure. We further employed X-ray photoelectron spectroscopy (XPS) to characterize the Cu₃P@C coating layer before and after cell cycling. The survey scans for the separator before and after cycles do not show obvious changes (Figure S14), indicating that the coating layer is electrochemically stable in Mg-S cells without any obvious side reactions. From the high-resolution spectra of Cu 2p (Figure 4d), before cycling the peaks at 952.6 and 932.7 eV correspond to Cu 2p_{1/2} and Cu 2p_{3/2} peaks of the Cu–P bond in Cu₃P, while the peaks at 954.8 and 934.3 eV are related to the Cu–O bond due to the surface oxidation resulting from exposure to air, as observed in previous studies.^{60,61} After cycling, the Cu–P peaks become stronger while the Cu–O peaks become weaker, further reflected in the appearance of a Cu–S peak (located at 936.5 eV), preliminarily indicating the binding or/and the partial reduction of polysulfides. The highly electro-negative O is conducive to create high-valence copper, chemically binding the negatively charged S sites of polysulfides via strong Cu–S bonding. The spectra of P 2p also display that the peak intensity of the P–Cu bond increases slightly as P–O bonds decrease (Figure 4e). This further verifies that the surface oxidation state of Cu–O–P species could activate the Cu sites for adsorbing and electrochemically converting Mg polysulfides, while Cu–O–P species could be partially reduced to the Cu–P state. Besides, we compared S 2p spectra of the cycled separator with pristine MgS_x (Figure 4f). It is found that the enhanced peak at 161.4 eV after cycling can be attributed to the formation of a Cu–S bond and a decrease is also found for the peak at 162.6 eV corresponding to the reduced polysulfides (PS).^{57,62} The growth of the S–O peak could be due to the impact from the electrolyte after cycling. These results match well with previous studies on Li-S

chemistry, in which some phosphides, such as FeP⁵³ and CoP,⁶³ with surface natural oxidation have a good catalytic effect on Li polysulfides to Li₂S₂/Li₂S.

To further understand the surface chemical bonding of PP-Cu₃P@C separators in Mg-S cells, we employed synchrotron soft X-ray adsorption spectroscopy (s-XAS) to evaluate the valence state of Cu in Cu₃P of the modified separator before and after cycling (as detailed in the Experimental Section). The s-XAS spectra were acquired in total electron yield (TEY) mode and total fluorescence yield (FY) mode. In general, the FY mode exhibits high sensitivity to the bulk of the material by probing a depth of 200 nm, while the TEY mode is surface-sensitive due to the short escape depth of electrons.^{64–66} For our materials, the obtained spectra (Figure 4g) show very small changes in FY mode but have a large shift in TEY mode, which means the surface chemistry of Cu₃P material changed after cycling. It is noted that a small peak shows up at 934.6 eV, which could be attributed to an increase of monovalent Cu species at the surface after cycling. The broad peak around 936–943 eV could result from low-valence Cu species such as a metallic Cu or Cu–S bond formed at the Cu₃P surface.^{64,67} These results match well with the XPS results, suggesting the surface oxidation state (Cu–O–P) on a Cu₃P particle could contribute to the gradually strong interactions with polysulfides with cycles, with few deep redox reactions inside its crystallized particles. Besides, the s-XAS spectrum (Figure S15) of the O K-edge presents a reduced peak (at 528 eV) after cycling in their TEY mode, while no obvious change is found in their FY mode, also suggesting that the reaction is limited to the surface. To better understand the conversion process, we demonstrate the function mechanism of catalytic Cu₃P in comparison to a conventional process (with a traditional separator) in Figure 4h. In a conventional process, S₈ is initially converted to Mg-PS intermediates, and these Mg-PS intermediates could dissolve in the electrolyte and shuttle to the anode because of a slow conversion to insoluble low-chain MgS₂ and MgS.

However, with the Cu_3P -based separator, the Cu_3P could realize a fast catalytic conversion of polysulfides to MgS_2/MgS due to the chemical binding of Mg-PS at the oxidation state surface (Cu-O-P) of Cu_3P nanoparticles. As a result, the dissolution and shuttle effect of the Mg-S cells are largely minimized.

Besides, the cycled Mg surface presents a relatively smooth surface without any dendrites or aggregates (Figure S16a), indicating a reversible deposition/dissolution of Mg/Mg^{2+} on the anode. From EDS mappings of the Mg surface, it was found that the S color is very weak, indicating a trace of polysulfide penetration through the separator. The EDS spectrum (Figure S16b) shows a strong Mg peak while S intensity is not obvious with a weight percentage of $\sim 1.87\%$ ($\sim 1.04\%$ atomic ratio, Figure S16c), which suggests that the shuttle effect from polysulfides has been mitigated. In contrast, the cycled Mg foil with a PP separator shows a large S content after cycling ($>4 \text{ wt } \%$ at its surface), as observed in the EDS mappings with an increase in S (Figure S17). To further evaluate the Mg anode plating/stripping process, we assembled Mg-Mg symmetric cells with $\text{PP-Cu}_3\text{P@C}$ and PP separators and cycled them with a plating/stripping areal current of 0.2 mA cm^{-2} for 0.5 h . As shown in Figure S18a,b, both cells can show reversible plating/stripping features for over 200 h , indicating a very stable electrochemistry for the $\text{Mg}[\text{B}(\text{Ohfp})_4]_2/\text{DME}$ -based electrolyte with the separators. The cell with the functional separator shows higher plating/stripping overpotentials than the PP cell during the initial cycles due to its relatively higher series resistance. However, the overpotentials of the PP cell decrease and then increase with cycles (Figure S17c), different from the gradually stabilized $\text{PP-Cu}_3\text{P@C}$ cell, which implies that the $\text{PP-Cu}_3\text{P@C}$ separator can stabilize the deposition/dissolution process of Mg on the anode.

Mg-S Cells at an Elevated Temperature. Battery operation in a wide temperature range is critical for practical applications. As such, we further explored whether the functional separator can improve cell performance at an elevated temperature. Figure 5a compares cycle stabilities of Mg-S cells with different PP and $\text{PP-Cu}_3\text{P@C}$ separators at 0.1 C under a 50°C environment. At a high temperature, the conversion reaction of S with Mg^{2+} will be accelerated due to the increased ionic conductivities of electrolyte and electrodes, but side reactions and polysulfide dissolution could become more serious. As a result, the Mg-S cells could exhibit higher specific capacity but relatively faster capacity decay at an elevated temperature compared to those running under room temperature. Initially, $\text{PP-Cu}_3\text{P@C}$ and PP cells respectively have initial capacities of 526 and 494 mAh g^{-1} (Figure 5a). After 200 cycles, the cell based on $\text{PP-Cu}_3\text{P@C}$ can maintain capacities over 383 mAh g^{-1} , much better than that with the uncoated separator (195 mAh g^{-1}). We also evaluated their rate capability within $0.1\text{--}1.0 \text{ C}$ at 50°C (Figure 5b). As expected, the cells show higher capacities at each rate compared to the tested results at room temperature. Compared to PP , the $\text{PP-Cu}_3\text{P@C}$ separator still enabled the cells to cycle better at 50°C . From 0.1 to 1.0 C , its discharge capacity varies from 500 to 260 mAh g^{-1} . By comparing their charge/discharge profiles at different rates (Figure 5c,d), we find the $\text{PP-Cu}_3\text{P@C}$ cell can maintain its magnesiation/demagnesiation plateaus at all rates, while the PP cell shows gradually disappearing plateaus with large voltage hysteresis as the rate increases, which indicates the functionalized separator

maintains the enhanced reversibility of Mg-S cells even at a high temperature. This could be attributed to the adsorptive and catalytic $\text{Cu}_3\text{P@C}$ layer that can minimize the shuttle effect from polysulfides and promote the electrochemical conversion of Mg polysulfides, and its high thermal stability and wettability can also provide advantages for Mg-S cells operating at elevated temperatures.

Additionally, we assembled Mg-S pouch cells with the functionalized separator to demonstrate its practical use. As shown in Figure 5e and Video S1 in the Supporting Information, a pouch cell can successfully light three LED lights. From a preliminary test of long-term cycling, our pouch cell can be charged/discharged at 0.1 C for over 100 cycles (Figure S19). In spite of these promising results, the Mg-S pouch cell is still a prototype and needs to be further optimized. With future technical optimizations, we expect that the Cu_3P -functionalized separators will enable stable cycling of the Mg-S pouch cells.

CONCLUSION

Current Mg-S batteries face challenges from the shuttle effect that originates from the dissolution of magnesium polysulfide, leading to several issues such as rapid capacity fading, large overcharge, high self-discharge, and potential safety concerns. A functionalized separator containing $\text{Cu}_3\text{P@C}$ layer has been developed to address these issues through adsorbing magnesium polysulfides and catalyzing the conversion reaction toward stable cycle life. The bifunctional layer with Cu_3P confined in a carbon matrix is coated on a commercial polypropylene membrane to form a porous membrane with high electrolyte wettability and good thermal stability. Density functional theory (DFT) calculations and polysulfide permeability tests reveal that Cu_3P can adsorb polysulfides via surface binding, largely reducing their dissolution and minimizing the shuttle effect. As a result, the Mg-S cells can achieve a high specific capacity of $\sim 450 \text{ mAh g}^{-1}$ at 0.1 C , fast rates, and a long cycle life (up to 500 cycles at 0.5 C), as well as stable performance even at an elevated temperature of 50°C . Different characterizations combined with a post-mortem analysis allow us to get insight into the function mechanism of the Cu_3P -based separator. We find that the surface oxidation state of Cu_3P could provide a surface interaction with polysulfides and quickly convert them into insoluble MgS_2/MgS , enhancing the electrochemical reversibility of Mg-S cells. Our study demonstrates an effective strategy for the design and functionalization of separators to realize the stable cycling of Mg-S batteries.

EXPERIMENTAL SECTION

Synthesis of $\text{Cu}_3\text{P@C}$ Micro-Octahedra. The $\text{Cu}_3\text{P@C}$ micro-octahedra were synthesized by the carbonization and phosphidation of a copper benzene-1,3,5-tricarboxylate (Cu-BTC) metal-organic framework (MOF). The Cu-BTC micro-octahedra were produced based on a typical coprecipitation process.⁴⁴ In brief, 0.875 g of benzene-1,3,5-tricarboxylic acid (H_3BTC) and 1.82 g of $\text{Cu}(\text{NO}_3)_2 \cdot 3\text{H}_2\text{O}$ were respectively dissolved in 50 mL of methanol under ultrasonication to form two homogeneous solutions. The obtained blue solution ($\text{Cu}(\text{NO}_3)_2 \cdot 3\text{H}_2\text{O}/\text{methanol}$) was poured into the transparent solution ($\text{H}_3\text{BTC}/\text{methanol}$) to form a mixture, and the mixture was then kept at room temperature for a precipitation process. After 2 h , the precipitates were retrieved by centrifugation, washed with methanol, and dried under vacuum. The Cu-BTC was carbonized in a tube furnace with an argon flow at 500°C for 2 h . After carbonization, a black powder (Cu@C) was obtained, and then

it was mixed with sodium hypophosphite ($\text{NaH}_2\text{PO}_3 \cdot \text{H}_2\text{O}$) at a mass ratio of 1:20, placed in a horizontal porcelain crucible, and heated at 350 °C in a tube furnace under an argon atmosphere for 2 h. After cooling, the product ($\text{Cu}_3\text{P}@C$) was collected and kept under vacuum for future use.

Fabrication of Functional Separator Membranes. The functional separator was fabricated via a slurry-coating method. As-produced $\text{Cu}_3\text{P}@C$ powder was mixed with carbon black and poly(vinylidene fluoride)-*co*-hexafluoropropylene (PVDF-HFP) with a mass ratio of 9:0.5:0.5 in *N*-methyl-2-pyrrolidone (NMP) to form a homogeneous slurry. The slurry was coated onto a PP (Celgard 2400) membrane using a doctor blade and then dried at 80 °C under vacuum overnight. After drying, the membrane was cut into disks (19 mm in diameter) for separator use. Compared to the glass fiber membranes as the separator in Mg-S batteries,^{39,57} the PP membrane is more soft and flexible, which allow a uniform Cu_3P coating layer on the surface via a doctor blade casting method. The resulting coating layer could have a stable adhesion to the PP surface without any cracks.

Synthesis of S/CMK-3 Composite. In a typical process, 0.7 g of sulfur was ball-milled with 1.75 g of CMK-3 at a mass ratio of 4:1 in a PTFE jar with agate balls under an Ar atmosphere. The mixture was heated in a closed quartz tube at 160 °C for 16 h and further heated at 400 °C for 1 h.

Materials Characterization. The phase structure was identified using X-ray diffraction (XRD, X'pert PRO, Alpha-1) with Cu K α radiation at 40 kV/40 mA. The morphology and microstructure were investigated using scanning electron microscopy (SEM, Hitachi SU8010) and transmission electron microscopy (TEM, FEI Tecnai G2 F30). The Brunauer–Emmett–Teller (BET) surface area and porosity of obtained samples were analyzed with an ASAP 2020 instrument (Micromeritics). Thermogravimetric analysis (TGA) was conducted with a thermal analyzer (Q600, TA Instruments). Contact angles were tested by a Drop Shape Analyzer (DSA 30, Kruss) with a drop of the electrolyte solution. The valence state and chemical composition were tested using an X-ray photoelectron spectrometer (XPS, Kratos Analytical Ltd.), an ultraviolet–visible (UV–vis) spectrophotometer (EV 300), and an energy dispersive X-ray spectrometer (EDS, Tecnai G2 F30). Soft X-ray adsorption spectroscopy (s-XAS) measurements were conducted at beamline 13-3 of the SSRL. The incident beams of oxygen and copper energy ranges were monochromatized by 600 and 1100 lines mm^{-1} spherical grating monochromators (SGMs), respectively. The incident angle was set as 30° from the sample surface. All of the s-XAS spectra were normalized by the intensity of the incoming beam, which was measured as a drain current on an electrically isolated gold-coated mesh simultaneously.

Preparation of Electrolyte. A Mg-S electrolyte based on $\text{Mg}[\text{B}(\text{Ohfp})_4]_2$ (magnesium tetrakis(hexafluoroisopropoxy)-borate) in DME (1,2-dimethoxyethane) was prepared via the method described in a previous study,⁵⁶ and all of the procedures were performed in an argon-filled glovebox ($\text{H}_2\text{O}/\text{O}_2 < 0.1$ ppm). Briefly, 0.55 mL of hexafluoroisopropanol (hfp-OH) was added dropwise to a solution of $\text{Mg}(\text{Bu})_2/\text{hexane}$ (2.5 mmol, 10 mL). The formed product $\text{Mg}(\text{Ohfp})_2$ was dissolved in 5.5 mL of $\text{BH}_3 \cdot \text{THF}$ and stirred for 30 min and 2 mL of hfp-OH dropped slowly into the above solution. The mixture was vigorously stirred overnight at 25 °C. After that, the solvent and excess hfp-OH were removed by vacuum heating at 50 °C for several hours. The resulted powder product was further dissolved in 5 mL of DME.

Assembly of Mg-S Coin Cells. The cell assembly process was conducted in an argon-filled glovebox (~ 0.1 ppm $\text{O}_2/\text{H}_2\text{O}$ level). CR2032 type Mg-S coin cells consisted of a Mg anode, a S/CMK-3 cathode, 0.5 M $\text{Mg}[\text{B}(\text{Ohfp})_4]_2/\text{DME}$ electrolyte, and PP (Celgard 2400) or PP- $\text{Cu}_3\text{P}@C$ separator. The S/CMK-3 electrode was prepared based on a slurry-casting process. In brief, the as-produced S@CMK-3 composite was mixed with Super-P and PVDF at a mass ratio of 8:1:1 in NMP to form a homogeneous slurry. The slurry was coated onto a carbon-coated Al foil using a doctor blade and then dried at 80 °C under vacuum overnight. The coated foil was cut into

disks (diameter of ~ 15 mm, areal loading of ~ 1 mg cm^{-2}) as the cathode, and Mg metal (diameter of ~ 15 mm) was used as the anode. The assembled cells rested under ambient conditions overnight before electrochemical tests.

Assembly of Mg-S Pouch Cells. To assemble pouch cells, a large sheet of the S@CMK-3 electrode with dimensions of 5.4 cm \times 3.4 cm was used as the cathode with an 0.508 mg cm^{-2} areal loading of sulfur. Mg foil with dimensions of 6 \times 4 cm^2 and a PP- $\text{Cu}_3\text{P}@C$ separator membrane with dimensions of 6.5 \times 4.5 cm^2 were sealed to the pouch.

Electrochemical Tests. The electrochemical performance of assembled cells was evaluated based on cyclic voltammetry (CV), electrochemical impedance spectroscopy (EIS), and galvanostatic charge–discharge (GCD) methods. The CV and EIS of these cells were determined with an electrochemical workstation (CHI650E, Chenhua, Shanghai), and GCD was determined with a LAND battery test system. The specific capacities of the cells were calculated based on the mass of sulfur from TGA results.

DFT Calculations. The Vienna ab initio simulation package (VASP) was employed for the density functional theory (DFT) calculations within the generalized gradient approximation (GGA).^{47–49} The projected augmented wave (PAW) potentials were used to describe the ionic cores and take valence electrons into account using a plane wave basis set with a kinetic energy cutoff of 450 eV.^{68,69} A geometry optimization was considered convergent when the force change was smaller than 0.05 eV/Å. Grimme's DFT-D3 methodology was used to describe the dispersion interactions.⁷⁰ The DFT + *U* correction for strong-correlation 3d electrons of transition metal was taken into account, and a *U*-*J* value of 3.87 for Cu was used.

ASSOCIATED CONTENT

Supporting Information

The Supporting Information is available free of charge at <https://pubs.acs.org/doi/10.1021/acsnano.2c09302>.

Video of a Mg-S pouch cell with the functional separator lighting three LED lights (MP4)

XRD, SEM, TGA, and BET of produced samples, SEM and photo of PP separator, calculated energies for different MgS_x interactions, DFT calculation model and DOS, SEM and EDS mappings and TGA for the S/CMK-3 composite, charge–discharge, CV, and EIS plots for Mg-S cells with different separators, XPS and soft XAS spectra of O K-edge for the cycled separator, SEM and EDS for the cycled Mg foil, plating/stripping cycles of $\text{Mg}||\text{Mg}$ symmetric cells, and cycle stability of Mg-S pouch cells (PDF)

AUTHOR INFORMATION

Corresponding Author

Yanna NuLi – School of Chemistry and Chemical Engineering, Shanghai Electrochemical Energy Devices Research Center, Shanghai Jiao Tong University, Shanghai 200240, People's Republic of China; orcid.org/0000-0003-0604-8550; Email: nlyn@sjtu.edu.cn

Authors

Yang Yang – School of Chemistry and Chemical Engineering, Shanghai Electrochemical Energy Devices Research Center, Shanghai Jiao Tong University, Shanghai 200240, People's Republic of China; orcid.org/0000-0002-9054-8525

Wenbin Fu – School of Materials Science and Engineering, Georgia Institute of Technology, Atlanta, Georgia 30332, United States; orcid.org/0000-0001-7539-3767

Duo Zhang – School of Chemistry and Chemical Engineering, Shanghai Electrochemical Energy Devices Research Center, Shanghai Jiao Tong University, Shanghai 200240, People's Republic of China

Wen Ren – School of Chemistry and Chemical Engineering, Shanghai Electrochemical Energy Devices Research Center, Shanghai Jiao Tong University, Shanghai 200240, People's Republic of China; orcid.org/0000-0002-1461-6717

Shuxin Zhang – School of Chemistry and Chemical Engineering, Shanghai Electrochemical Energy Devices Research Center, Shanghai Jiao Tong University, Shanghai 200240, People's Republic of China; orcid.org/0000-0001-5280-1529

Yuantao Yan – School of Chemistry and Chemical Engineering, Shanghai Electrochemical Energy Devices Research Center, Shanghai Jiao Tong University, Shanghai 200240, People's Republic of China

Yang Zhang – School of Chemistry and Chemical Engineering, Shanghai Electrochemical Energy Devices Research Center, Shanghai Jiao Tong University, Shanghai 200240, People's Republic of China

Sang-Jun Lee – Stanford Synchrotron Radiation Lightsource, SLAC National Accelerator Laboratory, Menlo Park, California 94025, United States; orcid.org/0000-0002-8199-3993

Jun-Sik Lee – Stanford Synchrotron Radiation Lightsource, SLAC National Accelerator Laboratory, Menlo Park, California 94025, United States; orcid.org/0000-0003-0181-9352

Zi-Feng Ma – School of Chemistry and Chemical Engineering, Shanghai Electrochemical Energy Devices Research Center, Shanghai Jiao Tong University, Shanghai 200240, People's Republic of China; orcid.org/0000-0001-5002-9766

Jun Yang – School of Chemistry and Chemical Engineering, Shanghai Electrochemical Energy Devices Research Center, Shanghai Jiao Tong University, Shanghai 200240, People's Republic of China; orcid.org/0000-0002-5270-3803

Jiulin Wang – School of Chemistry and Chemical Engineering, Shanghai Electrochemical Energy Devices Research Center, Shanghai Jiao Tong University, Shanghai 200240, People's Republic of China; orcid.org/0000-0001-8165-0096

Complete contact information is available at:
<https://pubs.acs.org/10.1021/acsnano.2c09302>

Notes

The authors declare no competing financial interest.

ACKNOWLEDGMENTS

This work was partially supported by the National Natural Science Foundation of China (Nos. 21975159, 21573146), the China Postdoctoral Science Foundation (No. 2021M702116), the Shanghai Aerospace Science and Technology Innovation Fund (No. SAST2018-117), and the Oceanic Interdisciplinary Program of Shanghai Jiao Tong University (No. WH410260401/006). The DFT calculations were performed on a TianHe-2 computer at the Shanxi Supercomputing Center of China. The soft X-ray adsorption measurements were carried out at the SSRL (beamline 13-3), SLAC National Accelerator Laboratory, supported by the U.S. Department of Energy, Office of Science, Office of Basic Energy Sciences, under Contract No. DE-AC02-76SF00515.

REFERENCES

- (1) Nitta, N.; Wu, F.; Lee, J. T.; Yushin, G. Li-Ion Battery Materials: Present and Future. *Mater. Today* **2015**, *18*, 252–264.
- (2) Whittingham, M. S. Lithium Batteries: 50 Years of Advances to Address the Next 20 Years of Climate Issues. *Nano Lett.* **2020**, *20*, 8435–8437.
- (3) Turcheniuk, K.; Bondarev, D.; Singhal, V.; Yushin, G. Ten Years Left to Redesign Lithium-Ion Batteries. *Nature* **2018**, *559*, 467–470.
- (4) Yoo, H. D.; Shterenberg, I.; Gofer, Y.; Gershtinsky, G.; Pour, N.; Aurbach, D. Mg Rechargeable Batteries: an On-Going Challenge. *Energy Environ. Sci.* **2013**, *6*, 2265–2279.
- (5) Nunes, S. C.; de Zea Bermudez, V.; Silva, M. M.; Barros, S.; Smith, M. J.; Morales, E.; Carlos, L. D.; Rocha, J. Di-Ureasil Ormolytes Doped with Mg²⁺ Ions: Part 1: Morphological, Thermal and Electrochemical Properties. *Solid State Ionics* **2005**, *176*, 1591–1599.
- (6) Fleischer, M. Recent Estimates of the Abundances of the Elements in the Earth's Crust. *Geological Survey Circular*; US Department of the Interior: 1953; Vol. 285, pp 1–6.
- (7) Niu, J.; Zhang, Z.; Aurbach, D. Alloy Anode Materials for Rechargeable Mg Ion Batteries. *Adv. Energy Mater.* **2020**, *10*, 2000697.
- (8) Goodenough, J. B.; Park, K.-S. The Li-Ion Rechargeable Battery: A Perspective. *J. Am. Chem. Soc.* **2013**, *135*, 1167–1176.
- (9) Muldoon, J.; Bucur, C. B.; Gregory, T. Quest for Nonaqueous Multivalent Secondary Batteries: Magnesium and Beyond. *Chem. Rev.* **2014**, *114*, 11683–11720.
- (10) Aurbach, D.; Lu, Z.; Schechter, A.; Gofer, Y.; Gizbar, H.; Turgeman, R.; Cohen, Y.; Moshkovich, M.; Levi, E. Prototype Systems for Rechargeable Magnesium Batteries. *Nature* **2000**, *407*, 724–727.
- (11) Levi, E.; Gofer, Y.; Aurbach, D. On the Way to Rechargeable Mg Batteries: The Challenge of New Cathode Materials. *Chem. Mater.* **2010**, *22*, 860–868.
- (12) Ma, Z.; MacFarlane, D. R.; Kar, M. Mg Cathode Materials and Electrolytes for Rechargeable Mg Batteries: A Review. *Batteries Supercaps* **2019**, *2*, 115–127.
- (13) Mao, M.; Gao, T.; Hou, S.; Wang, C. A Critical Review of Cathodes for Rechargeable Mg Batteries. *Chem. Soc. Rev.* **2018**, *47*, 8804–8841.
- (14) Yuan, H.; Yang, Y.; NuLi, Y.; Yang, J.; Wang, J. A Conductive Selenized Polyacrylonitrile Cathode in Nucleophilic Mg²⁺/Li⁺ Hybrid Electrolytes for Magnesium-Selenium Batteries. *J. Mater. Chem. A* **2018**, *6*, 17075–17085.
- (15) Wu, D.; Ren, W.; NuLi, Y.; Yang, J.; Wang, J. Recent Progress on Selenium-Based Cathode Materials for Rechargeable Magnesium Batteries: A Mini Review. *J. Mater. Sci. Technol.* **2021**, *91*, 168–177.
- (16) Nguyen, D.-T.; Horia, R.; Eng, A. Y. S.; Song, S.-W.; Seh, Z. W. Material Design Strategies to Improve the Performance of Rechargeable Magnesium-Sulfur Batteries. *Mater. Horiz.* **2021**, *8*, 830–853.
- (17) Ye, C.; Chao, D.; Shan, J.; Li, H.; Davey, K.; Qiao, S.-Z. Unveiling the Advances of 2D Materials for Li/Na-S Batteries Experimentally and Theoretically. *Matter* **2020**, *2*, 323–344.
- (18) Pope, M. A.; Aksay, I. A. Structural Design of Cathodes for Li-S Batteries. *Adv. Energy Mater.* **2015**, *5*, 1500124.
- (19) Yang, Y.; Wang, W.; Nuli, Y.; Yang, J.; Wang, J. High Active Magnesium Trifluoromethanesulfonate-Based Electrolytes for Magnesium-Sulfur Batteries. *ACS Appl. Mater. Interfaces* **2019**, *11*, 9062–9072.
- (20) Zhao-Karger, Z.; Fichtner, M. Magnesium-Sulfur Battery: Its Beginning and Recent Progress. *MRS Commun.* **2017**, *7*, 770–784.
- (21) Gao, T.; Hou, S.; Wang, F.; Ma, Z.; Li, X.; Xu, K.; Wang, C. Reversible S⁰/MgS_x Redox Chemistry in a MgTFSI₂/MgCl₂/DME Electrolyte for Rechargeable Mg/S Batteries. *Angew. Chem., Int. Ed.* **2017**, *56*, 13526–13530.
- (22) Xu, Y.; Ye, Y.; Zhao, S.; Feng, J.; Li, J.; Chen, H.; Yang, A.; Shi, F.; Jia, L.; Wu, Y.; Yu, X.; Glans-Suzuki, P.-A.; Cui, Y.; Guo, J.; Zhang, Y. In Situ X-Ray Absorption Spectroscopic Investigation of the

Capacity Degradation Mechanism in Mg/S Batteries. *Nano Lett.* **2019**, *19*, 2928–2934.

(23) Huang, X. L.; Wang, Y.-X.; Chou, S.-L.; Dou, S. X.; Wang, Z. M. Materials Engineering for Adsorption and Catalysis in Room-Temperature Na-S Batteries. *Energy Environ. Sci.* **2021**, *14*, 3757–3795.

(24) Bai, S.; Liu, X.; Zhu, K.; Wu, S.; Zhou, H. Metal-Organic Framework-Based Separator for Lithium-Sulfur Batteries. *Nat. Energy* **2016**, *1*, 16094.

(25) Wang, P.; Buchmeiser, M. R. Rechargeable Magnesium-Sulfur Battery Technology: State of the Art and Key Challenges. *Adv. Funct. Mater.* **2019**, *29*, 1905248.

(26) Zhou, X.; Tian, J.; Hu, J.; Li, C. High Rate Magnesium-Sulfur Battery with Improved Cyclability Based on Metal-Organic Framework Derivative Carbon Host. *Adv. Mater.* **2018**, *30*, 1704166.

(27) Zhang, S.; Ren, W.; NuLi, Y.; Wang, B.; Yang, J.; Wang, J. Sulfurized-Pyrolyzed Polyacrylonitrile Cathode for Magnesium-Sulfur Batteries Containing $\text{Mg}^{2+}/\text{Li}^{+}$ Hybrid Electrolytes. *Chem. Eng. J.* **2022**, *427*, 130902.

(28) Krishna, M.; Ghosh, A.; Muthuraj, D.; Das, S.; Mitra, S. Electrocatalytic Activity of Polyaniline in Magnesium-Sulfur Batteries. *J. Phys. Chem. Lett.* **2022**, *13*, 1337–1343.

(29) Gao, T.; Noked, M.; Pearse, A. J.; Gillette, E.; Fan, X.; Zhu, Y.; Luo, C.; Suo, L.; Schroeder, M. A.; Xu, K.; Lee, S. B.; Rubloff, G. W.; Wang, C. Enhancing the Reversibility of Mg/S Battery Chemistry through Li^{+} Mediation. *J. Am. Chem. Soc.* **2015**, *137*, 12388–12393.

(30) Wei, C.; Tan, L.; Zhang, Y.; Xi, B.; Xiong, S.; Feng, J.; Qian, Y. Highly Reversible Mg Metal Anodes Enabled by Interfacial Liquid Metal Engineering for High-Energy Mg-S Batteries. *Energy Storage Mater.* **2022**, *48*, 447–457.

(31) Li, R.; Liu, Q.; Zhang, R.; Li, Y.; Ma, Y.; Huo, H.; Gao, Y.; Zuo, P.; Wang, J.; Yin, G. Achieving High-Energy-Density Magnesium/Sulfur Battery via a Passivation-Free Mg-Li Alloy Anode. *Energy Storage Mater.* **2022**, *50*, 380–386.

(32) Zhang, S. S. A Review on the Separators of Liquid Electrolyte Li-Ion Batteries. *J. Power Sources* **2007**, *164*, 351–364.

(33) Orendorff, C. J. The Role of Separators in Lithium-Ion Cell Safety. *Electrochem. Soc. Interface* **2012**, *21*, 61–65.

(34) Klein, S.; Wrogemann, J. M.; van Wickeren, S.; Harte, P.; Bärmann, P.; Heidrich, B.; Hesper, J.; Borzutzki, K.; Nowak, S.; Börner, M.; Winter, M.; Kasnatscheew, J.; Placke, T. Understanding the Role of Commercial Separators and Their Reactivity toward LiPF_6 on the Failure Mechanism of High-Voltage NCM523 || Graphite Lithium Ion Cells. *Adv. Energy Mater.* **2022**, *12*, 2102599.

(35) Zhang, X.; Sahraei, E.; Wang, K. Deformation and Failure Characteristics of Four Types of Lithium-Ion Battery Separators. *J. Power Sources* **2016**, *327*, 693–701.

(36) Jeong, Y. C.; Kim, J. H.; Nam, S.; Park, C. R.; Yang, S. J. Rational Design of Nanostructured Functional Interlayer/Separator for Advanced Li-S Batteries. *Adv. Funct. Mater.* **2018**, *28*, 1707411.

(37) Huang, X.; He, R.; Li, M.; Chee, M. O. L.; Dong, P.; Lu, J. Functionalized Separator for Next-Generation Batteries. *Mater. Today* **2020**, *41*, 143–155.

(38) Yu, X.; Manthiram, A. Performance Enhancement and Mechanistic Studies of Room-Temperature Sodium-Sulfur Batteries with a Carbon-Coated Functional Nafion Separator and a Na_2S /Activated Carbon Nanofiber Cathode. *Chem. Mater.* **2016**, *28*, 896–905.

(39) Ji, Y.; Liu-Théato, X.; Xiu, Y.; Indris, S.; Njel, C.; Maibach, J.; Ehrenberg, H.; Fichtner, M.; Zhao-Karger, Z. Polyoxometalate Modified Separator for Performance Enhancement of Magnesium-Sulfur Batteries. *Adv. Funct. Mater.* **2021**, *31*, 2100868.

(40) Wang, L.; Jankowski, P.; Njel, C.; Bauer, W.; Li, Z.; Meng, Z.; Dasari, B.; Vegge, T.; Lastra, J. M. G.; Zhao-Karger, Z.; Fichtner, M. Dual Role of Mo_6S_8 in Polysulfide Conversion and Shuttle for Mg-S Batteries. *Adv. Sci.* **2022**, *9*, 2104605.

(41) Zhao, X.; Kong, X.; Liu, Z.; Li, Z.; Xie, Z.; Wu, Z.; He, F.; Chang, X.; Yang, P.; Zheng, J.; Li, X. The Cutting-Edge Phosphorus-

Rich Metal Phosphides for Energy Storage and Conversion. *Nano Today* **2021**, *40*, 101245.

(42) Yang, Y.; Fu, W.; Bell, C.; Lee, D.-C.; Drexler, M.; Nuli, Y.; Ma, Z.-F.; Magasinski, A.; Yushin, G.; Alamgir, F. M. Iron Phosphide Confined in Carbon Nanofibers as a Free-Standing Flexible Anode for High-Performance Lithium-Ion Batteries. *ACS Appl. Mater. Interfaces* **2021**, *13*, 34074–34083.

(43) Yu, F.; Zhou, H.; Huang, Y.; Sun, J.; Qin, F.; Bao, J.; Goddard, W. A.; Chen, S.; Ren, Z. High-Performance Bifunctional Porous Non-Noble Metal Phosphide Catalyst for Overall Water Splitting. *Nat. Commun.* **2018**, *9*, 2551.

(44) Wu, R.; Qian, X.; Yu, F.; Liu, H.; Zhou, K.; Wei, J.; Huang, Y. MOF-Templated Formation of Porous CuO Hollow Octahedra for Lithium-Ion Battery Anode Materials. *J. Mater. Chem. A* **2013**, *1*, 11126–11129.

(45) Furukawa, H.; Cordova, K. E.; O’Keeffe, M.; Yaghi, O. M. The Chemistry and Applications of Metal-Organic Frameworks. *Science* **2013**, *341*, 1230444.

(46) Tovar, T. M.; Zhao, J.; Nunn, W. T.; Barton, H. F.; Peterson, G. W.; Parsons, G. N.; LeVan, M. D. Diffusion of CO_2 in Large Crystals of Cu-BTC MOF. *J. Am. Chem. Soc.* **2016**, *138*, 11449–11452.

(47) Kresse, G.; Furthmüller, J. Efficiency of Ab-Initio Total Energy Calculations for Metals and Semiconductors Using a Plane-Wave Basis Set. *Comput. Mater. Sci.* **1996**, *6*, 15–50.

(48) Kresse, G.; Furthmüller, J. Efficient Iterative Schemes for Ab Initio Total-Energy Calculations Using a Plane-Wave Basis Set. *Phys. Rev. B* **1996**, *54*, 11169–11186.

(49) Perdew, J. P.; Burke, K.; Ernzerhof, M. Generalized Gradient Approximation Made Simple. *Phys. Rev. Lett.* **1996**, *77*, 3865–3868.

(50) Manna, G.; Bose, R.; Pradhan, N. Semiconducting and Plasmonic Copper Phosphide Platelets. *Angew. Chem., Int. Ed.* **2013**, *52*, 6762–6766.

(51) Shen, R.; Xie, J.; Lu, X.; Chen, X.; Li, X. Bifunctional Cu_3P Decorated $\text{g-C}_3\text{N}_4$ Nanosheets as a Highly Active and Robust Visible-Light Photocatalyst for H_2 Production. *ACS Sustain. Chem. Eng.* **2018**, *6*, 4026–4036.

(52) Li, Z.; Li, H.; Wang, S.; Yang, F.; Zhou, W. Mesoporous Black $\text{TiO}_2/\text{MoS}_2/\text{Cu}_2\text{S}$ Hierarchical Tandem Heterojunctions toward Optimized Photothermal-Photocatalytic Fuel Production. *Chem. Eng. J.* **2022**, *427*, 131830.

(53) Shen, J.; Xu, X.; Liu, J.; Li, F.; Hu, R.; Liu, J.; Hou, X.; Feng, Y.; Yu, Y.; Zhu, M. Mechanistic Understanding of Metal Phosphide Host for Sulfur Cathode in High-Energy-Density Lithium-Sulfur Batteries. *ACS Nano* **2019**, *13*, 8986–8996.

(54) Sun, R.; Bai, Y.; Luo, M.; Qu, M.; Wang, Z.; Sun, W.; Sun, K. Enhancing Polysulfide Confinement and Electrochemical Kinetics by Amorphous Cobalt Phosphide for Highly Efficient Lithium-Sulfur Batteries. *ACS Nano* **2021**, *15*, 739–750.

(55) Zhao-Karger, Z.; Zhao, X.; Wang, D.; Diemant, T.; Behm, R. J.; Fichtner, M. Performance Improvement of Magnesium Sulfur Batteries with Modified Non-Nucleophilic Electrolytes. *Adv. Energy Mater.* **2015**, *5*, 1401155.

(56) Mandai, T. Critical Issues of Fluorinated Alkoxyborate-Based Electrolytes in Magnesium Battery Applications. *ACS Appl. Mater. Interfaces* **2020**, *12*, 39135–39144.

(57) Zhao-Karger, Z.; Liu, R.; Dai, W.; Li, Z.; Diemant, T.; Vinayan, B. P.; Bonatto Minella, C.; Yu, X.; Manthiram, A.; Behm, R. J.; Ruben, M.; Fichtner, M. Toward Highly Reversible Magnesium-Sulfur Batteries with Efficient and Practical $\text{Mg}[\text{B}(\text{hfp})_4]_2$ Electrolyte. *ACS Energy Lett.* **2018**, *3*, 2005–2013.

(58) Sun, J.; Deng, C.; Bi, Y.; Wu, K.-H.; Zhu, S.; Xie, Z.; Li, C.; Amal, R.; Luo, J.; Liu, T.; Wang, D.-W. In Situ Sulfurized Carbon-Confined Cobalt for Long-Life Mg/S Batteries. *ACS Appl. Energy Mater.* **2020**, *3*, 2516–2525.

(59) Bi, Y.; He, S.; Fan, C.; Luo, J.; Yuan, B.; Liu, T. L. A Robust Ionic Liquid Magnesium Electrolyte Enabling Mg/S Batteries. *J. Mater. Chem. A* **2020**, *8*, 12301–12305.

(60) Zhao, R.; Geng, Q.; Chang, L.; Wei, P.; Luo, Y.; Shi, X.; Asiri, A. M.; Lu, S.; Wang, Z.; Sun, X. Cu₃P Nanoparticle-Reduced Graphene Oxide Hybrid: an Efficient Electrocatalyst to Realize N₂-to-NH₃ Conversion under Ambient Conditions. *Chem. Commun.* **2020**, 56, 9328–9331.

(61) Wang, R.; Dong, X.-Y.; Du, J.; Zhao, J.-Y.; Zang, S.-Q. MOF-Derived Bifunctional Cu₃P Nanoparticles Coated by a N,P-Codoped Carbon Shell for Hydrogen Evolution and Oxygen Reduction. *Adv. Mater.* **2018**, 30, 1703711.

(62) Muthuraj, D.; Pandey, M.; Krishna, M.; Ghosh, A.; Sen, R.; Johari, P.; Mitra, S. Magnesium Polysulfide Catholyte (MgS_x): Synthesis, Electrochemical and Computational Study for Magnesium-Sulfur Battery Application. *J. Power Sources* **2021**, 486, 229326.

(63) Zhong, Y.; Yin, L.; He, P.; Liu, W.; Wu, Z.; Wang, H. Surface Chemistry in Cobalt Phosphide-Stabilized Lithium-Sulfur Batteries. *J. Am. Chem. Soc.* **2018**, 140, 1455–1459.

(64) Vegelius, J. R.; Kvashnina, K. O.; Hollmark, H.; Klintonberg, M.; Kvashnin, Y. O.; Soroka, I. L.; Werme, L.; Butorin, S. M. X-ray Spectroscopic Study of Cu₂S, CuS, and Copper Films Exposed to Na₂S Solutions. *J. Phys. Chem. C* **2012**, 116, 22293–22300.

(65) Li, S.; Qian, G.; He, X.; Huang, X.; Lee, S.-J.; Jiang, Z.; Yang, Y.; Wang, W.-N.; Meng, D.; Yu, C.; Lee, J.-S.; Chu, Y. S.; Ma, Z.-F.; Pianetta, P.; Qiu, J.; Li, L.; Zhao, K.; Liu, Y. Thermal-Healing of Lattice Defects for High-Energy Single-Crystalline Battery Cathodes. *Nat. Commun.* **2022**, 13, 704.

(66) Yogi, C.; Takamatsu, D.; Yamanaka, K.; Arai, H.; Uchimoto, Y.; Kojima, K.; Watanabe, I.; Ohta, T.; Ogumi, Z. Soft X-Ray Absorption Spectroscopic Studies with Different Probing Depths: Effect of an Electrolyte Additive on Electrode Surfaces. *J. Power Sources* **2014**, 248, 994–999.

(67) Hollmark, H. M.; Keech, P. G.; Vegelius, J. R.; Kristiansen, P.; Werme, L.; Duda, L. C. Sulfidation of Oxidized Copper Studied by Soft X-ray Spectroscopy. *MRS Proceedings* **2012**, 1475, 459–464.

(68) Blöchl, P. E. Projector Augmented-Wave Method. *Phys. Rev. B* **1994**, 50, 17953–17979.

(69) Kresse, G.; Joubert, D. From Ultrasoft Pseudopotentials to the Projector Augmented-Wave Method. *Phys. Rev. B* **1999**, 59, 1758–1775.

(70) Grimme, S.; Antony, J.; Ehrlich, S.; Krieg, H. A Consistent and Accurate Ab Initio Parametrization of Density Functional Dispersion Correction (DFT-D) for the 94 Elements H-Pu. *J. Chem. Phys.* **2010**, 132, 154104.

Recommended by ACS

Tuning the Local Coordination of CoP_{1-x}S_x between NiAs- and MnP-Type Structures to Catalyze Lithium–Sulfur Batteries

Zihan Shen, Huigang Zhang, *et al.*

JANUARY 30, 2023

ACS NANO

READ 

Hexagonal Carbon Nanoplates Decorated with Layer-Engineered MoS₂: High-Performance Cathode Materials for Zinc-Ion Batteries

Chang Wan Kang, Seung Uk Son, *et al.*

FEBRUARY 02, 2023

ACS APPLIED MATERIALS & INTERFACES

READ 

Redox Promotion by Prelithiation Modification of the Separator in Lithium–Sulfur Batteries

Qiumi Huang, Chengyang Wang, *et al.*

FEBRUARY 20, 2023

THE JOURNAL OF PHYSICAL CHEMISTRY C

READ 

Bifunctional Photoassisted Li–O₂ Battery with Ultrahigh Rate-Cycling Performance Based on Siloxene Size Regulation

Congying Jia, Zong-Huai Liu, *et al.*

JANUARY 09, 2023

ACS NANO

READ 

Get More Suggestions >